



HAL
open science

The Origin of the Doppler Flip in HD 100546: A Large-scale Spiral Arm Generated by an Inner Binary Companion

Brodie J. Norfolk, Christophe Pinte, Josh Calcino, Iain Hammond, Nienke van der Marel, Daniel J. Price, Sarah T. Maddison, Valentin Christiaens, Jean-François Gonzalez, Dori Blakely, et al.

► To cite this version:

Brodie J. Norfolk, Christophe Pinte, Josh Calcino, Iain Hammond, Nienke van der Marel, et al.. The Origin of the Doppler Flip in HD 100546: A Large-scale Spiral Arm Generated by an Inner Binary Companion. The Astrophysical journal letters, 2022, 936, 10.3847/2041-8213/ac85ed . insu-03777331

HAL Id: insu-03777331

<https://insu.hal.science/insu-03777331>

Submitted on 14 Sep 2022

HAL is a multi-disciplinary open access archive for the deposit and dissemination of scientific research documents, whether they are published or not. The documents may come from teaching and research institutions in France or abroad, or from public or private research centers.

L'archive ouverte pluridisciplinaire **HAL**, est destinée au dépôt et à la diffusion de documents scientifiques de niveau recherche, publiés ou non, émanant des établissements d'enseignement et de recherche français ou étrangers, des laboratoires publics ou privés.



Distributed under a Creative Commons Attribution 4.0 International License



The Origin of the Doppler Flip in HD 100546: A Large-scale Spiral Arm Generated by an Inner Binary Companion

Brodie J. Norfolk¹ , Christophe Pinte^{2,3} , Josh Calcino⁴ , Iain Hammond² , Nienke van der Marel⁵ , Daniel J. Price² , Sarah T. Maddison¹ , Valentin Christiaens⁶ , Jean-François Gonzalez⁷ , Dori Blakely⁸ , Giovanni Rosotti^{5,9} , and Christian Ginski⁵

¹ Centre for Astrophysics and Supercomputing (CAS), Swinburne University of Technology, Hawthorn, Victoria 3122, Australia; bnorfolk@swin.edu.au

² School of Physics and Astronomy, Monash University, Vic 3800, Australia

³ Univ. Grenoble Alpes, CNRS, IPAG, F-38000 Grenoble, France

⁴ Theoretical Division, Los Alamos National Laboratory, Los Alamos, NM 87545, USA

⁵ Leiden Observatory, Niels Bohrweg 2, 2333 CA Leiden, The Netherlands

⁶ Space sciences, Technologies & Astrophysics Research (STAR) Institute, Université de Liège, Allée du Six Août 19c, B-4000 Sart Tilman, Belgium
⁷ Univ Lyon, Univ Claude Bernard Lyon 1, ENS de Lyon, CNRS, Centre de Recherche Astrophysique de Lyon UMR5574, F-69230, Saint-Genis-Laval, France

⁸ University of Victoria, 3800 Finnerty Road, Victoria, BC, V8P 5C2, Canada

⁹ School of Physics and Astronomy, University of Leicester, Leicester, LE1 7RH, UK

Received 2022 April 29; revised 2022 July 14; accepted 2022 August 2; published 2022 August 26

Abstract

Companions at subarcsecond separation from young stars are difficult to image. However, their presence can be inferred from the perturbations they create in the dust and gas of protoplanetary disks. Here we present a new interpretation of SPHERE polarized observations that reveal the previously detected inner spiral in the disk of HD 100546. The spiral coincides with a newly detected ¹²CO inner spiral and the previously reported CO emission Doppler flip, which has been interpreted as the signature of an embedded protoplanet. Comparisons with hydrodynamical models indicate that this Doppler flip is instead the kinematic counterpart of the spiral, which is likely generated by an inner companion inside the disk cavity.

Unified Astronomy Thesaurus concepts: [Protoplanetary disks \(1300\)](#)

1. Introduction

High-resolution observations from ALMA and VLT Spectro-Polarimetric High contrast imager for Exoplanets REsearch (SPHERE) have revealed that numerous transition disks contain spirals that propagate in altitude from millimeter grains in the midplane up to micrometer grains in the upper layers of the disk (e.g., V1247 Ori, HD 135355B, MWC 758, HD 100453; Kraus et al. 2017; Cazzoletti et al. 2018; Dong et al. 2018; Rosotti et al. 2020). Observing these spirals and spiral-induced features (e.g., non-Keplerian motion) in disks (for $M_{\text{disk}} \leq 10\% M_{\text{star}}$; Toomre 1964) presents strong evidence for the presence of a disk-perturbing companion (Dong et al. 2015; Pinte et al. 2018a; Calcino et al. 2022).

2. Methods

2.1. IRDIS Polarimetric Observations

The disk surrounding HD 100546 (distance: 108.12 ± 0.44 pc, age: $5.5_{-0.8}^{+1.4}$ Myr, mass: $2.05_{-0.12}^{+0.10} M_{\odot}$; Gaia Collaboration et al. 2021; Vioque et al. 2018) contains a large spiral arm in the inner disk and spirals at larger scales as seen in scattered-light observations (Garufi et al. 2016; Follette et al. 2017; Sissa et al. 2018). It also harbors a Doppler flip, i.e., a sign reversal in the ¹²CO rotation map at ~ 20 au from the star where the Keplerian rotation has been subtracted (Casassus & Pérez 2019; Pérez et al. 2020, hereafter CP19, CP20). CP19 and CP20 suggested that these deviations from Keplerian rotation might be the

imprint of a $>5 M_{\text{Jup}}$ embedded protoplanet, where the Doppler flip arises from the opposite signs of the velocity field, relative to the planet, in the inner and outer Lindblad resonance spirals.

However, as discussed by the authors, the planet origin for the non-Keplerian motions is difficult to reconcile with the submillimeter continuum observations. The Doppler flip, and hence the tentative planet, is colocated with the azimuthal asymmetry seen in the dust continuum ring, while massive embedded planets are expected to carve gaps in the dust (and gas) distribution (e.g., Paardekooper & Mellema 2004).

In this Letter, we compare SPHERE *H*-band scattered-light images with ALMA ¹²CO $J=2-1$ observations and present hydrodynamical and radiative transfer models to explore whether the disk central cavity (~ 16.5 au) and CO kinematic structure share a common origin, namely a close companion carving the cavity and generating spiral arms.

HD 100546 was observed with the Infrared Differential Imaging Spectrometer (IRDIS; Dohlen et al. 2008) instrument on the SPHERE (Beuzit et al. 2008) on 2019 February 18 as part of ESO program 0102.C-0162(A) (PI: C. Ginski). We used the dual-polarization imaging (PDI) mode (de Boer et al. 2020), with an integration time of 16 s, an *H*-band filter (1.625 μm), and an apodized Lyot coronagraph ALC2 (N_{ALC_YJH_S}, diameter 185 mas). We used eight polarimetric cycles with two exposures at each half-wave plate position (total integration time 17 minutes) with an average seeing of $0''.82$ (after excluding the first polarimetric cycle and several cycles that showed inconsistent coronographic status).

We reduced the archival observations (unpublished) using the IRDIS Data reduction for Accurate Polarimetry pipeline (IRDAP; van Holstein et al. 2020). We computed the clean *Q* and *U* Stokes parameters using the normalized double-difference method and corrected for instrument polarization



Original content from this work may be used under the terms of the [Creative Commons Attribution 4.0 licence](#). Any further distribution of this work must maintain attribution to the author(s) and the title of the work, journal citation and DOI.

by applying the Mueller matrix model. A $Q_\phi r^2$ -scaled image was produced using `diskmap` (Stolker et al. 2016) to account for stellocentric flux loss to 150 au, using the revised Gaia distance of 110 ± 0.6 pc and disk inclination 43.2° and PA 144° retrieved from Markov Chain Monte Carlo fits of the submillimeter continuum emission.

2.2. ALMA Observations and Data Reduction

We calibrated archival ALMA Band 6 observations (projects: 2016.1.00344.S, published in CP19 and CP20; and 2018.1.01309.S, published in Casassus et al. 2022) using the CASA pipeline for the appropriate ALMA cycle. Continuum observations have a total bandwidth of 2 GHz for 2016.1.00344.S and 6 GHz for 2018.1.01309.S. The ^{13}CO and $\text{C}^{18}\text{O } J=2-1$ lines were observed with a resolution of 122 kHz in the 2016.1.00344.S program, and the $^{12}\text{CO } J=2-1$ line was observed at 122 kHz resolution in both programs. We performed four rounds of phase-only self-calibration on the continuum short baseline data of 2016.1.00344.S with successive integration times of “*inf.*” 120 s, 60 s, and “*int.*” For the long baseline continuum data of both programs, we performed a single phase-only self-calibration with an infinite integration time. We shifted each execution to a common position with the “*fixvis*” task and rescaled the flux of the long baseline visibilities to match the short baseline data using the DSHARP reduction utilities, prior to concatenating all the executions. We applied the same self-calibration solutions, shifting and rescaling to the CO lines.

The continuum and CO emission were imaged using the *telean* task in CASA, with the Multiscale Clean deconvolver (Cornwell 2008) with Briggs weighting. We used a robust parameter of 0.5 for the continuum, leading to a beam size of $0''.03 \times 0''.02$, with a PA of 31° , a signal-to-noise ratio (S/N) of 320 and rms of $9.8 \mu\text{Jy beam}^{-1}$. For the ^{12}CO emission (with and without continuum subtraction) we used a channel width of 0.32 km s^{-1} , a robust parameter of 1.0, and a *uv* taper of $0''.06$ resulting in a beam size of $0''.95 \times 0''.081$, with a PA of 16° and an rms noise of $0.8 \text{ mJy beam}^{-1}$ for our continuum-subtracted cube, and beam size $0''.094 \times 0''.081$, PA of 18° , and rms noise of $1.0 \text{ mJy beam}^{-1}$ for our nonsubtracted cube. We then applied JvM (Jorsater & van Moorsel 1995) and primary beam corrections to all images. For ^{13}CO and C^{18}O emission (continuum subtracted), we used a channel width of 0.32 km s^{-1} , a robust parameter of 1.0, and a *uv* taper of $0''.06$. This resulted in a beam size of $0''.12 \times 0''.10$, with a PA of -20° and an rms noise of $1.7 \text{ mJy beam}^{-1}$ for ^{13}CO , and a beam size of $0''.12 \times 0''.10$, with a PA of -19° and a rms noise of $1.3 \text{ mJy beam}^{-1}$ for C^{18}O .

2.3. Hydrodynamics and Radiative Transfer Modeling

We performed 3D smoothed particle hydrodynamics (SPH) simulations using PHANTOM (Price et al. 2018a). Our goal was not to perform a detailed fitting of all the available observations, but to explore if a binary can explain both the central cavity and disrupted kinematics. We assumed a central star with mass $2 M_\odot$ (Vioque et al. 2018). Based on previous work on synthetic observations of circumbinary disks (Ragusa et al. 2017; Price et al. 2018a), we only explored a restricted region of the parameter space with companion masses between 0.2 and $0.6 M_\odot$ ($q = 0.1$ and 0.3) at a semimajor axis of 8.4 au (e.g., $\sim 1/2 \times$ the cavity radius of ~ 16.2 au; Artymowicz &

Lubow 1994) and on orbits with eccentricities between 0.2 and 0.6. We treated both stars as sink particles (Bate et al. 1995) with accretion radii of 0.7 au. We initialized a gas-only circumbinary disk with 2×10^6 SPH particles between $R_{\text{in}} = 16.8$ au and $R_{\text{out}} = 126$ au, with a surface density profile $\Sigma(r) \propto r^{-1}$, a temperature profile $T \propto r^{-0.5}$, and a scale height $H/R_{\text{ref}} = 0.05$ at $R_{\text{ref}} = 25.2$ au (chosen to closely match the scale height of the disk; see Appendix D, where $(H/R)_{^{12}\text{CO}} \approx 3 - 4 \times H/R_{\text{ref}}$). We used a total gas disk mass of $5 \times 10^{-3} M_\odot$. Given this low mass we neglect the disk self-gravity. We modeled the disk viscosity using an average Shakura & Sunyaev (1973) viscosity of $\alpha_{\text{SS}} = 5 \times 10^{-3}$ by setting the SPH artificial viscosity $\alpha_{\text{AV}} = 0.24$.

Length values are given after a rescaling of all length (and consequentially velocity and time) code units in our PHANTOM models to match the models cavity radius with the observed cavity radius (e.g., ~ 16 au; Pérez et al. 2020).

We ran our models for 100 orbits of the central binary and then reran them for one additional orbit with outputs every 1/10 of an orbit to study how the disk structure varies as a function of the binary phase. Although the duration of our simulation is lower than the viscous timescale, circumbinary disk simulations by Hirsh et al. (2020) show that the cavity size is largely set on timescales of a few hundred binary orbits.

For each of the 10 output samples along the final orbit of our SPH simulations, we generated a Voronoi mesh for input into the Monte Carlo radiative transfer code MCFOST (Pinte et al. 2006, 2009), which is used to produce synthetic CO emission observations. We assumed a power-law dust grain size distribution $dn/ds \propto s^{-3.5}$ for $0.05 \mu\text{m} \leq s \leq 3000 \mu\text{m}$ with a gas-to-dust ratio of 20 (Bruderer et al. 2012 suggest a ratio of 100 is a better fit to their Herschel data; however, their alternative solution of Gas/Dust = 20 is in closer agreement with more recent derivations using ALMA data; Miley et al. 2019) for a population of spherical and homogeneous grains composed of astronomical silicate (Weingartner & Draine 2001). We set $T_{\text{eff}} = 10,250$ and $R_\odot = 1.91$ for HD 100546 as derived by Vioque et al. (2018). We assumed that our companion is approximately the same age as its host (e.g., 5 Myr; Vioque et al. 2018) and used the isochrones from Siess et al. (2000), which led to effective temperatures of 3870 K and a radii of $1.16 R_\odot$. We used an initial CO abundance of $\text{CO}/\text{H}_2 = 1 \times 10^{-4}$. This ratio is affected by freeze-out when $T < 20$ K (depletion factor of 1×10^{-4}), full photodissociation by UV radiation, as well as photodesorption of the CO ice (following Appendix B of Pinte et al. 2018a). We generated channel maps with a spectral resolution of 0.32 km s^{-1} and convolved them by the observed beam. The resulting synthetic cubes do not reproduce the observed peak temperature (~ 130 K versus ~ 180 K); however, this likely indicates that $T_{\text{gas}} \geq T_{\text{dust}}$ in the CO-emitting layer, due to, for instance, PAH photoelectric heating (Woitke et al. 2009), which is not included here. A similar difference was observed by de Gregorio-Monsalvo et al. (2013) for HD 163296.

3. Results and Discussion

3.1. The Doppler Flip is the Kinematic Counterpart of a Spiral Arm

We redetect a large-scale spiral in scattered light (Figure 1, left panel) originating from the inner edge of the disk ($\approx 0''.12$) in the southeast direction and opening to the north up to $\approx 0''.25$ separation (previously imaged by Garufi et al. 2016; Follette et al. 2017; Sissa et al. 2018). We also detect this inner spiral

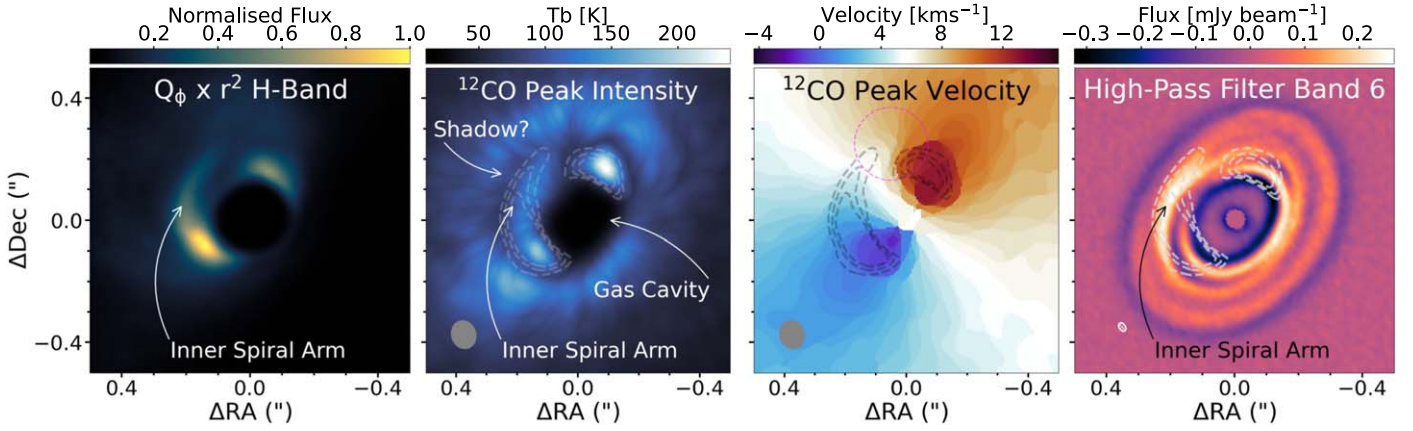


Figure 1. Panel 1: $Q_\phi r^2$ -scaled H -band observations with a sinh colorbar to emphasize bright emission. Panel 2: inner region of the ^{12}CO non-continuum-subtracted peak intensity map; a sinh colorbar is used to emphasize the bright inner gas spiral. Panel 3: peak velocity map of continuum-subtracted ^{12}CO emission. The magenta dashed circle represents the location of the Doppler flip reported by CP19. Panel 4: our Band 6 continuum observations with a high-pass filter. We masked the bright unresolved inner disk to highlight the emission structure in the ring component; see Appendix A for further details. Overplotted in each panel are the black/white dashed contours from the SPHERE observations at 0.53, 0.61, and 0.69 normalized flux units.

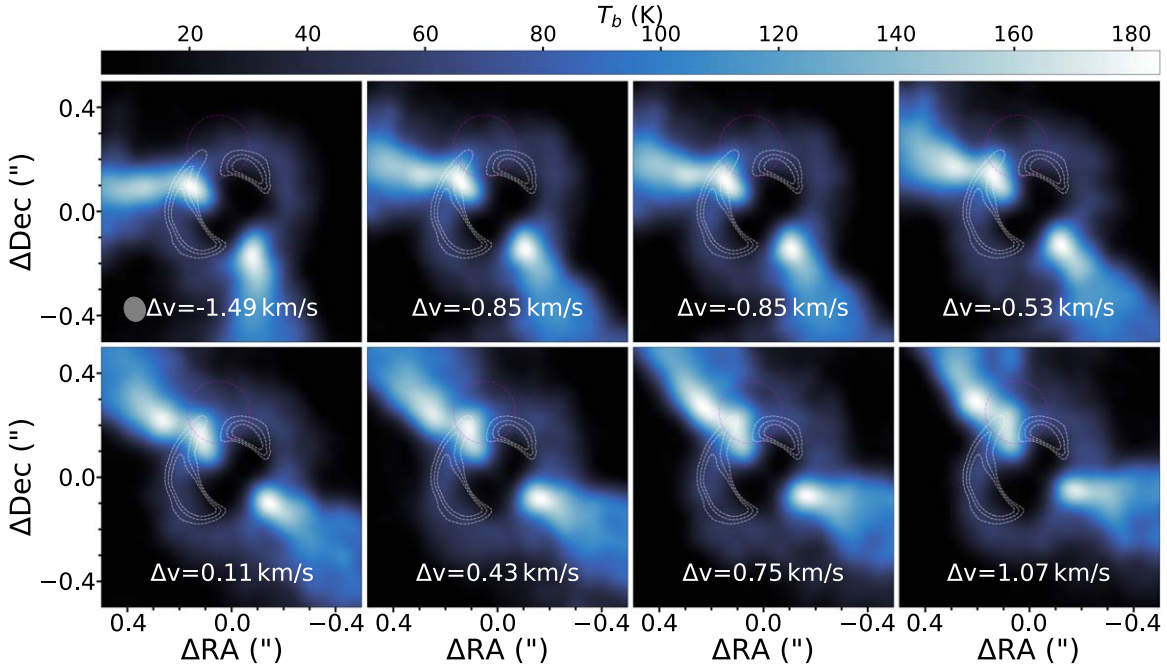


Figure 2. Selected non-continuum-subtracted $^{12}\text{CO } J=2-1$ channel maps highlighting the deviation from Keplerian velocity at the edge of the disk cavity. The lower limit on the colorbar is set to 15 K. The SPHERE Q_ϕ image is shown with white dashed contours at 1.3e6, 1.5e6, and 1.7e6 au. White arrows point to the “kink” as it shifts across each channel map. The magenta dashed circle represents the location of the Doppler flip reported by CP19.

arm in non-continuum-subtracted ^{12}CO peak brightness temperature (second panel) and a tentative shadow behind the spiral (both the spiral and shadow are detected in the continuum-subtracted cube albeit to a lesser extent). The scattered-light spiral aligns with this newly detected gas spiral as well as the bending of the isovelocity curves in the ^{12}CO peak velocity map (third panel), i.e., with what appears as the Doppler flip in the $v_{\text{Keplerian}}$ -subtracted rotation map in CP19 (Figure 1). Equivalently, the scattered-light spiral is colocated with the velocity kinks observed in the channel maps (Figure 2), which is also tentatively seen in ^{13}CO and C^{18}O emission (e.g., see Appendix C).

Because scattered light and ^{12}CO emission arise from similar altitudes in the disk (e.g., see Appendix D), projection effects should be minimal, which suggests that the scattered-light

spiral is likely to be physically connected to the non-Keplerian motions observed in ^{12}CO .

We observe evidence of additional cospatial features in the disk. Figure 3 highlights several deviations from Keplerian motion at large scales in the ^{12}CO channel maps, which includes a large kink in the $\Delta v = -0.85 \text{ m s}^{-1}$ and 0.53 km s^{-1} channels, also visible in our EDDY model subtraction residuals, that coincide with the outer scattered-light spiral arm (this connection is also detected in our ^{12}CO peak intensity map; see Appendix B for further details). Additionally, using a high-bandpass filter on the 1.3 mm dust continuum observations, we trace a tentative spiral structure (Figure 1, right panel) crossing the dust crescent at the inner edge of the cavity. Assuming sufficient dust settling and a relatively lower optical depth at

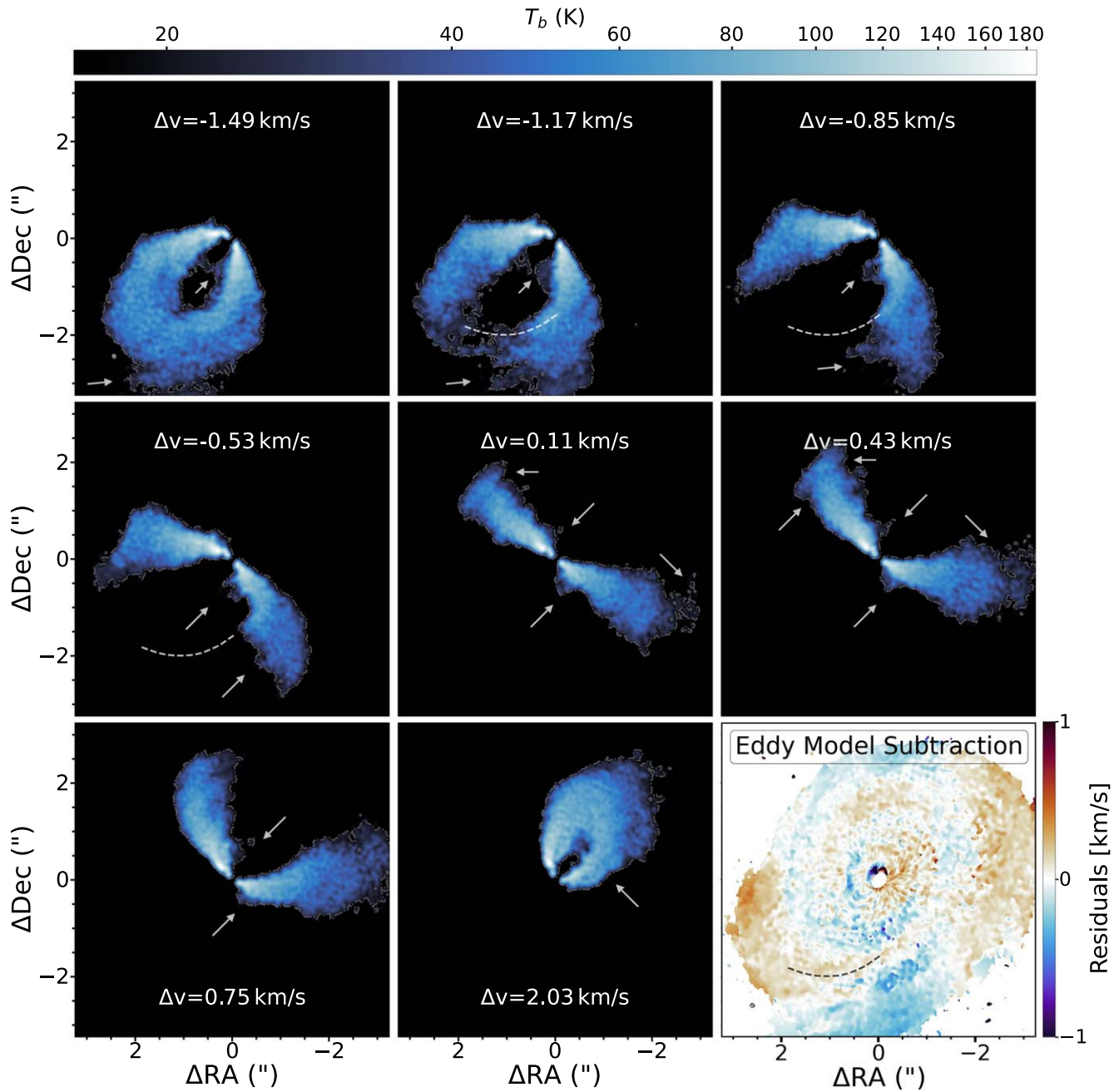


Figure 3. Large-scale continuum-subtracted CO(2–1) channel maps. We highlight several non-Keplerian features with white arrows and overlay a trace of the southern scattered-light spiral (see Figure 7) with a dashed line. We include a large-scale view of our EDDY model subtraction residuals and highlight with a dashed black contour that a prominent velocity spiral arm in the residual map also coincides with the scattered-light spiral. To ensure these deviations are not background noise, we plot the 5σ value ($5 \times 1.2 \text{ mJy beam}^{-1}$) with a dashed-dotted gray contour in each channel.

1.3 mm, this spiral structure is likely to be the midplane counterpart of the scattered-light spiral (as similarly found for HD 100453; Rosotti et al. 2020).

3.2. An Inner Binary Generates an Apparent Doppler Flip

Our modeling shows that a planet at ~ 20 au is not required to produce a kinematic structure that resembles the Doppler flip detected in HD 100546. The surface density of the SPH simulation with $q = 0.3$ ($M_{\text{binary}}/M_{\text{star}}$) and $e = 0.6$ (eccentricity) (our fiducial model) along with the corresponding ^{12}CO channel maps are shown in Figure 4. The central binary is able to produce the prominent spiral arms, with the associated non-Keplerian motions.

Our model displays several velocity kinks at the edge of the cavity, with amplitude and shape similar to those observed in HD 100546. As our goal is only to qualitatively explain the observations, we explored a limited region of the parameter space, and the selected model is not a unique solution. The amplitude of the kinematic deviation increases with mass ratio and eccentricity. Models with $q \leq 0.2$ did not perturb the disk sufficiently to produce the observed non-Keplerian motion, suggesting a stellar-mass companion was required. We note that a more massive companion might have led to an even better agreement with the observations, but a mass ratio of 0.3 is already in tension with the constraints of sparse aperture masking (see discussion in Section 3.3), so we did not explore higher masses.

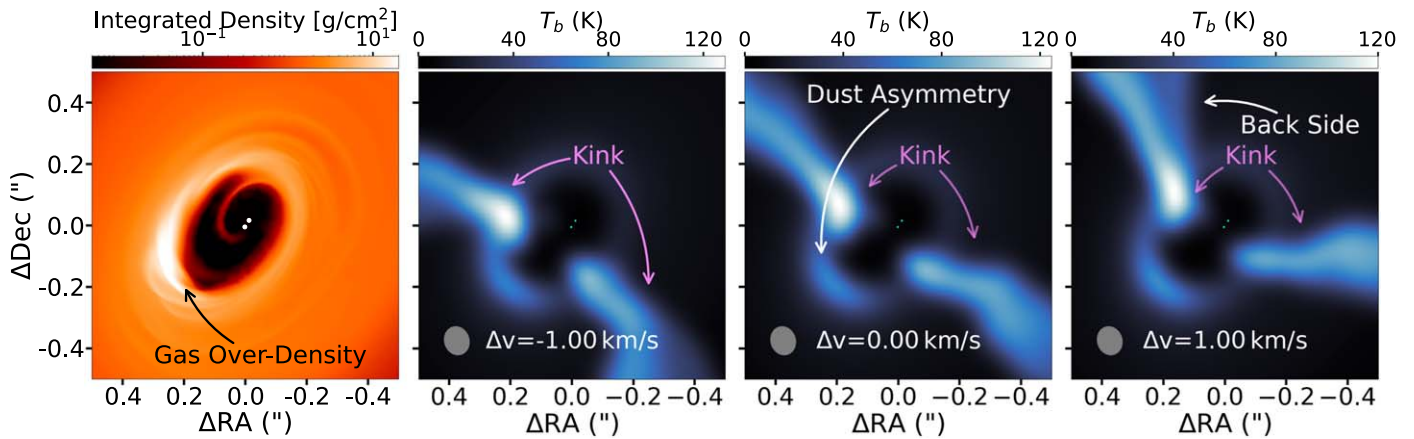


Figure 4. Panel 1: integrated density from our SPH simulation. Panels 2, 3, and 4: synthetic channel maps from our circumbinary model with a $\sim 0.6 M_{\odot}$ ($q = 0.3$) companion at 8.4 au convolved with the same beam dimensions as the observations.

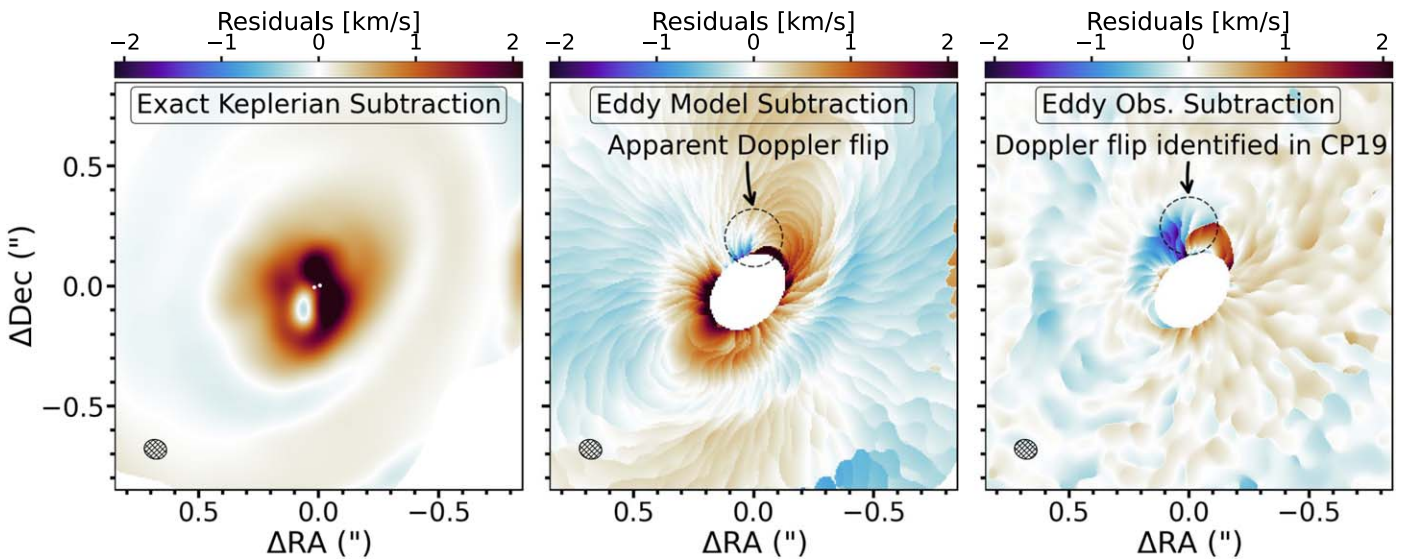


Figure 5. Left: residuals from the known Keplerian velocities, i.e., by subtracting a model where we force the gas velocities to be circular and Keplerian around the center of gravity of the model, assuming a central mass of $2.6 M_{\odot}$ (i.e., the total mass of the binary). Center: best-fit Keplerian rotation subtracted with eddy from moment 1 of our SPH simulation. Right: as in the center panel, but for the continuum-subtracted ^{12}CO observations of HD 100546 presented in this work. The binary induced spiral arms in our SPH simulation produce substantial deviations ($\sim 1 \text{ km s}^{-1}$) from Keplerian rotation over short distances, which appears like a Doppler flip when trying to subtract an estimated velocity field. This is similar to the deviations seen in HD 100546 by CP19.

To assess if the fiducial model’s kinematic structure can appear as a Doppler flip, we subtracted an “exact” Keplerian velocity field from the model peak velocity map (by forcing the SPH particles to be on a circular Keplerian orbit around a central object with a mass equal to the sum of the two binary objects) and present the residuals in Figure 5, panel 1 (adopting a procedure similar to that used in Pinte et al. 2020). The resulting velocity residuals reveal that the gas flow is strongly non-Keplerian, with velocity spirals at multiple scales, but do not show a Doppler flip at the edge of the cavity.

However, for the observed disk, the unperturbed velocity field is unknown and is instead estimated either by fitting a model (e.g., Teague et al. 2018) or by constructing an azimuthal average (CP19). We then perform a similar procedure on our synthetic observations, as well as on the observations (Figure 5, central and right panels). We generate a peak velocity map with BETTERMOMENTS (Teague & Foreman-Mackey 2018), before subtracting a Keplerian model using EDDY (Teague 2019). Both the synthetic and observed cubes are processed in the same way.

The right panel of Figure 5 shows a sign reversal in the rotation map that is consistent with the Doppler flip detected by CP19. Interestingly, we detect a similar flip in the synthetic observations (central panel) and spiral-like residuals. A comparison with the left panel shows that this apparent Doppler flip is an artifact of the subtraction procedure. EDDY tries to subtract a Keplerian rotation field that best matches the observations. This relies on the assumption that a smooth Keplerian rotation background dominates the velocity field. Consequentially for our synthetic residual map, EDDY slightly underestimates the central mass (2.4 instead of $2.6 M_{\odot}$). The subtraction of this estimated velocity average from the strongly modulated rotation map then results in an apparent sign reversal in the residuals.

3.3. Where is the Companion?

The similarity between the EDDY residuals for the ^{12}CO data and synthetic observations from the SPH simulation suggests that the Doppler flip detected by CP19 may simply be the summation of “kinks” across the systematic velocity that

remains after subtracting an average velocity background. We showed that the observed kinematic structures in HD 100546 (apparent Doppler flip, non-Keplerian motions in the cavity, CP20, initially reported as a misaligned inner gas disk; Walsh et al. 2017) can be explained by a central binary, rather than a planet located inside the dust ring. A central binary can also explain the presence of many of the structures observed by other disk tracers, such as the large cavity and asymmetry observed in continuum wavelengths (Pérez et al. 2020; Norfolk et al. 2021), the spiral arm seen in scattered light (Garufi et al. 2016; Follette et al. 2017; Sissa et al. 2018, and see our model comparison in Appendix E), as well as the non-Keplerian motions observed in the inner regions of the disk via SO emission (Booth et al. 2018). A single binary companion has been shown to drive similar disk features in both HD 142527 (Price et al. 2018b) and potentially IRS 48 (Calcino et al. 2019), although a companion has not been detected directly in the latter.

A series of observational studies have suggested the presence of a companion inside the cavity of HD 100546 (Brittain et al. 2014, 2019), although most have discussed a several-Jupiter-mass planet rather than a stellar-mass companion. CP20 conducted sparse aperture masking observations (SAM) with SPHERE and concluded that no stellar companion exists in the cavity. Our model predicts a apparent separation of 25 mas and a flux ratio of 8.4 ($\Delta M = 2.3$) in the K band between the two stars. According to the detection limits of the SPHERE SAM observations (Figure 6 in CP20), such a companion should have been detected. This discrepancy might be resolved with a lower-mass companion that is inclined relative to the outer disk. Inclined lower-mass companions will generate non-Keplerian motions at similar magnitudes (e.g., as was seen for the variety of inclinations used for HD 142527b’s orbit; Price et al. 2018b) while remaining undetected in the SAM observations. However, we did not consider inclined configurations in this study for simplicity. We also note that while the Gravity data reveal a large fractional contribution of the circumstellar disk in the VLTI field of view: 0.63 in the K band, the visibilities and phase closures display high-frequency modulations (Figure B.1 in Gravity Collaboration et al. 2019) that may indicate the presence of a companion. Gaia Collaboration et al. (2021) indicate a preliminary astrometric excess noise of 0.38 mas at the 155σ level, which is significantly larger than the 0.16 mas of HD 142527, where there is a known $\approx 0.2 M_{\odot}$ binary companion (Price et al. 2018a). While the astrometric signal in a young star can be perturbed by variability and illumination effects, making it difficult to definitely attribute any excess noise to a physical astrometric wobble caused by a companion, the large excess in HD 100546 does suggest the presence of a binary companion.

The short orbital period of a potential binary (about 15 yr in our model) also offers some exciting opportunities for monitoring to test our interpretation. For instance, our model predicts that for most of the binary orbit (7/10 dumps across 1 orbit), the velocity kink is flipped (at the same azimuthal position) compared to the current configuration. If our prediction is correct, kinematic signatures should change significantly over the next 3 to 5 yr, and regular ALMA follow-up observations could test the validity of our proposed binary–disk configuration. If the orbit is indeed eccentric, additional observations with SAM might also be able to reveal the companion within a few years.

Although a companion inside the cavity can explain the morphological features around the millimeter dust cavity, an additional mechanism might be required to explain features at large scales. A dust ring with radius ~ 180 au was reported by Fedele et al. (2021) and is potentially created by a massive planet at ~ 80 – 120 au. Such a planet could produce morphological and kinematic signatures such as localized kinks (e.g., Pinte et al. 2018a) or more extended velocity perturbations from spiral arms (Calcino et al. 2022). Another possibility is that the disk around HD 100546 is being perturbed by late-stage inflows (Dullemond et al. 2019). Either or both of these scenarios could explain the spiral arms and kinematic perturbations seen at distances larger than 100 au ($\gtrsim 1''$) from the central cavity in Figures 3 and 7. Interestingly, this is similar to HD 142527, where Garg et al. (2021) detected large-scale spirals up to 300 au while the central binary semimajor axis ranges from 12 to 31 au (Claudi et al. 2019).

4. Summary

1. Using archival SPHERE observations, we confirmed the prominent spiral arm stemming from the edge of the cavity, previously detected (Garufi et al. 2016; Follette et al. 2017; Sissa et al. 2018), and note that it spatially aligns with the “kink” observed in the ^{12}CO channel maps, or equivalently with the Doppler flip seen in the rotation map residuals.
2. Our hydrodynamical modeling shows that a $\sim 0.6 M_{\odot}$ ($q = 0.3$) companion at ≈ 8 au can reproduce many of the observed disk features, including an inner ^{12}CO cavity, a velocity kink, and corresponding residual Doppler flip (albeit at a weaker magnitudes) at the edge of the cavity, a scattered-light spiral, and a cavity and asymmetry in the millimeter dust.
3. We detect several new non-Keplerian features at large scales across the whole disk and at all velocities, some of which also appear to spatially coincide with spirals seen in scattered light, the origin of which remains unclear.

B.J.N. is supported by an Australian Government Research Training Program Scholarship. C.P. and D.P. acknowledge funding from the Australian Research Council via FT170100040 and DP180104235. J.-F.G. acknowledges funding from ANR (Agence Nationale de la Recherche) of France under contract number ANR-16-CE31-0013 (Planet-Forming-Disks). V.C. acknowledges funding from the Belgian F.R.S.-FNRS. This project has received funding from the European Union’s Horizon 2020 research and innovation program under the Marie Skłodowska-Curie grant agreements No 210021 and No 823823 (DUSTBUSTERS). G.R. acknowledges support from the Netherlands Organisation for Scientific Research (NWO, program number 016.Veni.192.233) and from an STFC Ernest Rutherford Fellowship (grant number ST/T003855/1). SPH simulations were performed on OzStar, funded by Swinburne University of Technology and the Australian government. The National Radio Astronomy Observatory is a facility of the National Science Foundation operated under agreement by the Associated Universities, Inc. ALMA is a partnership of ESO (representing its member states), NSF (USA) and NINS (Japan), together with NRC (Canada) and NSC and ASIAA (Taiwan) and KASI (Republic of Korea), in cooperation with the Republic of Chile. The Joint ALMA Observatory is operated by ESO,

AUI/ NRAO and NAOJ. This work has made use of data from the European Space Agency (ESA) mission Gaia (<https://www.cosmos.esa.int/gaia>), processed by the Gaia Data Processing and Analysis Consortium (DPAC; <https://www.cosmos.esa.int/web/gaia/dpac/consortium>). Funding for the DPAC has been provided by national institutions, in particular the institutions participating in the Gaia Multilateral Agreement.

Facilities: European Southern Observatory (ESO) 8.2m Very Large Telescope (VLT) Melipal (UT3 VISIR, SPHERE, VIMOS instruments) at Paranal Observatory.

Software: CASA (McMullin et al. 2007), IRDAP (van Holstein et al. 2020), PHANTOM (Price et al. 2018b), MCFOST (Pinte et al. 2006, 2009).

Appendix A ALMA Band 6 Continuum Observations

Here we present our Band 6 continuum observation in Figure 6 (left). We apply the high-pass filter by convolving the image with an inverse Gaussian kernel, defined in Fourier space as

$$K(\nu) = 1.0 - \exp\left(-\frac{\nu^2}{\sigma_\nu^2}\right), \quad (\text{A1})$$

where ν is the spatial frequency and σ_ν is the width of the filter, which we took to be 0.15 arcsec^{-1} . This effectively suppresses structure on scales larger than $0''.15$. Figure 6 (right) shows the resulting image.

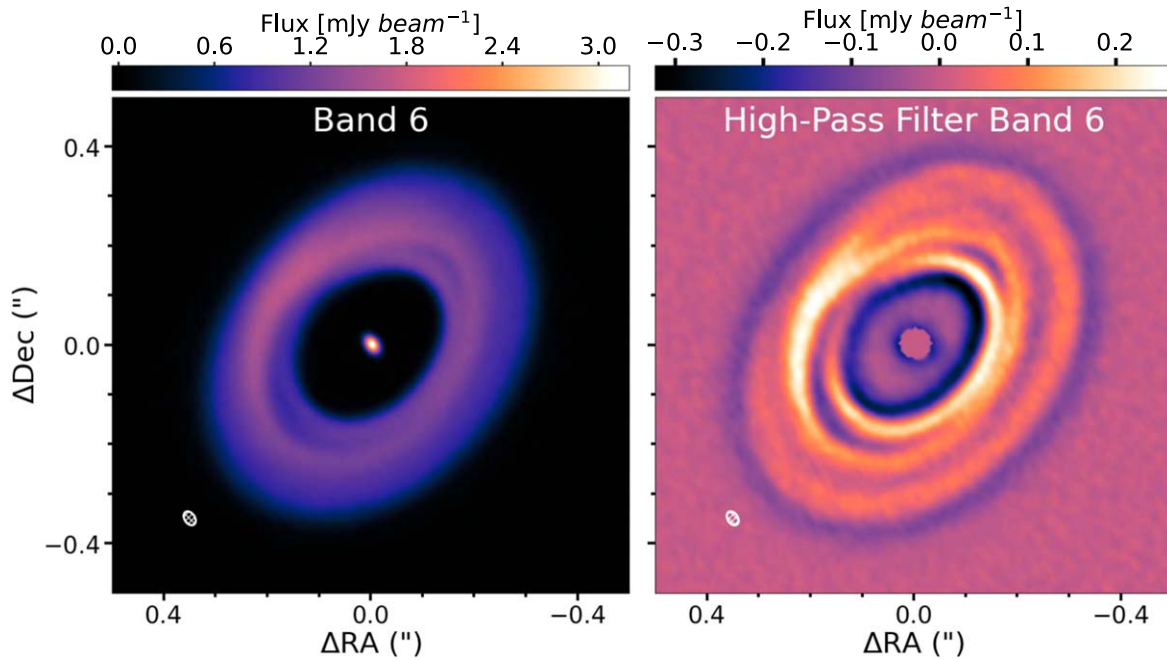


Figure 6. Left: our Band 6 observations. Right: our Band 6 continuum observations with a high-pass filter.

Appendix B Spirals at Large Scales

In Figure 7 we present a large-scale view of the scattered-light observations and the peak intensity map of the non-

continuum ^{12}CO emission, which highlights spiral structures at large radii. Our single binary model fails to reproduce these large-scale structures, suggesting that there likely exist other

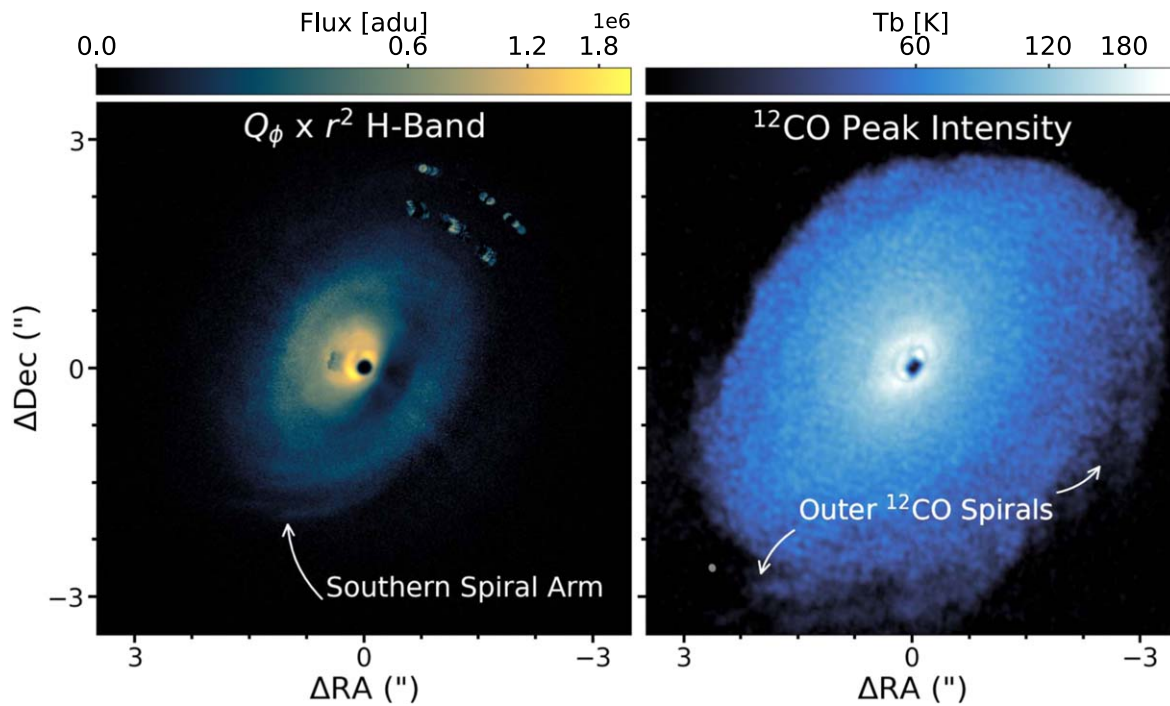


Figure 7. Left: $Q_\phi r^2$ H-band observations. Right: peak intensity map of ^{12}CO emission. An asinh scale is applied to both figures to highlight the fainter outer disk emission.

perturbing bodies farther out in the disk. The outer companion proposed to be driving the outer dust trap (Fedele et al. 2021) may also induce spirals at larger scales; however, further hydrodynamical models are required to constrain the perturber (s) mass and orbit.

Appendix C Non-Keplerian Motion Seen in ^{13}CO and C^{18}O

In Figure 8 we present the continuum-subtracted ^{13}CO and C^{18}O channel maps. Contrary to the findings of CP20 (see their

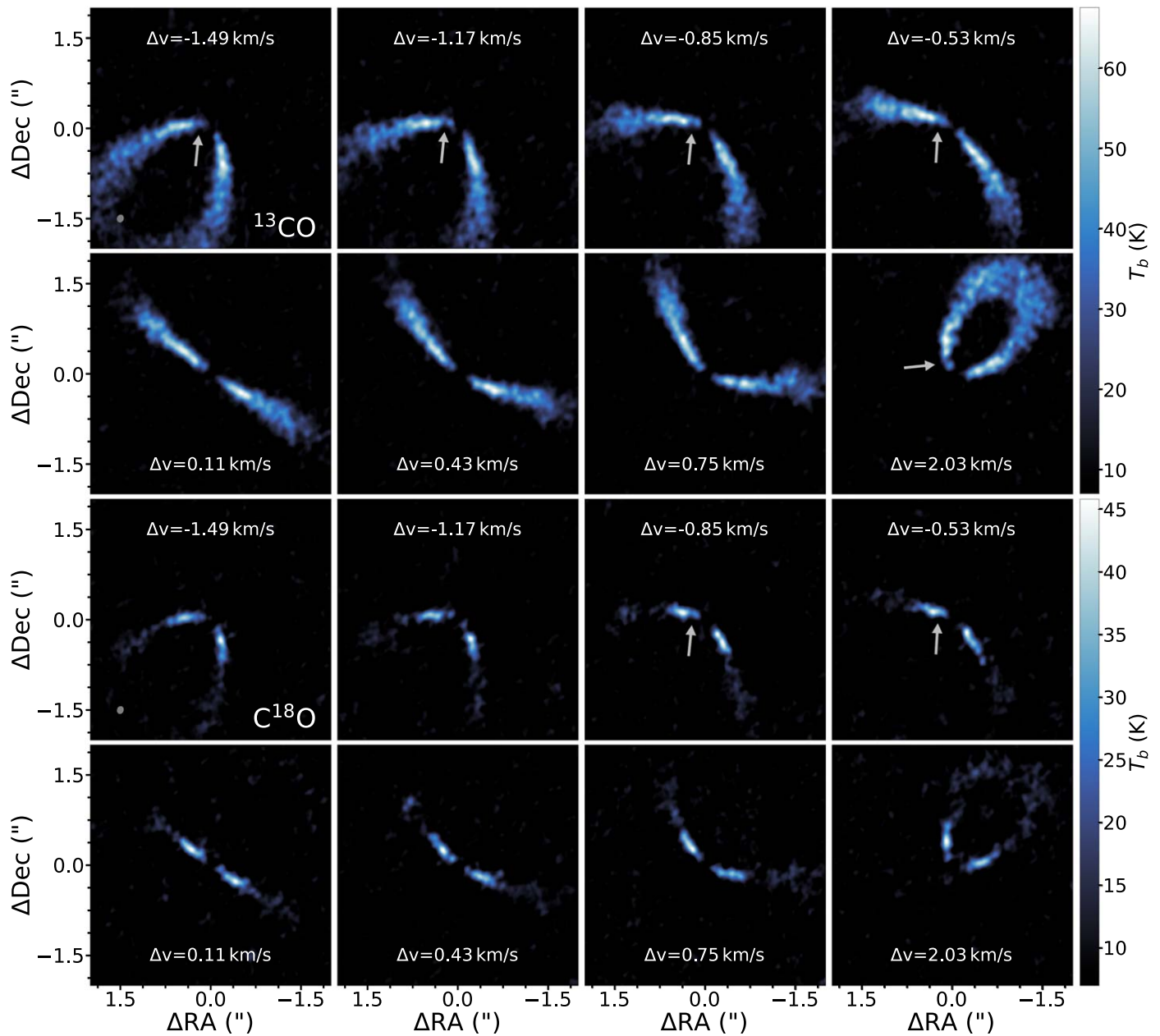


Figure 8. Large-scale continuum-subtracted ^{13}CO and C^{18}O channel maps. We highlight a tentative inner kink in both isotopologues with a white arrow.

Section 3.2.2), we find that ^{13}CO shows tentative non-Keplerian motion at small and large spatial scales, while the lower-S/N isotopologue C^{18}O exhibits a tentative inner kink in only a few channels. The tentative inner kink in ^{13}CO and C^{18}O spatially corresponds to the strong inner kink seen in ^{12}CO ; we highlight this feature in both isotopologues with a white arrow.

Appendix D Comparing the Altitude of ^{12}CO and Scattered-light Emission

To compare the location of substructures from various disk tracers, we need to evaluate the respective emission heights to

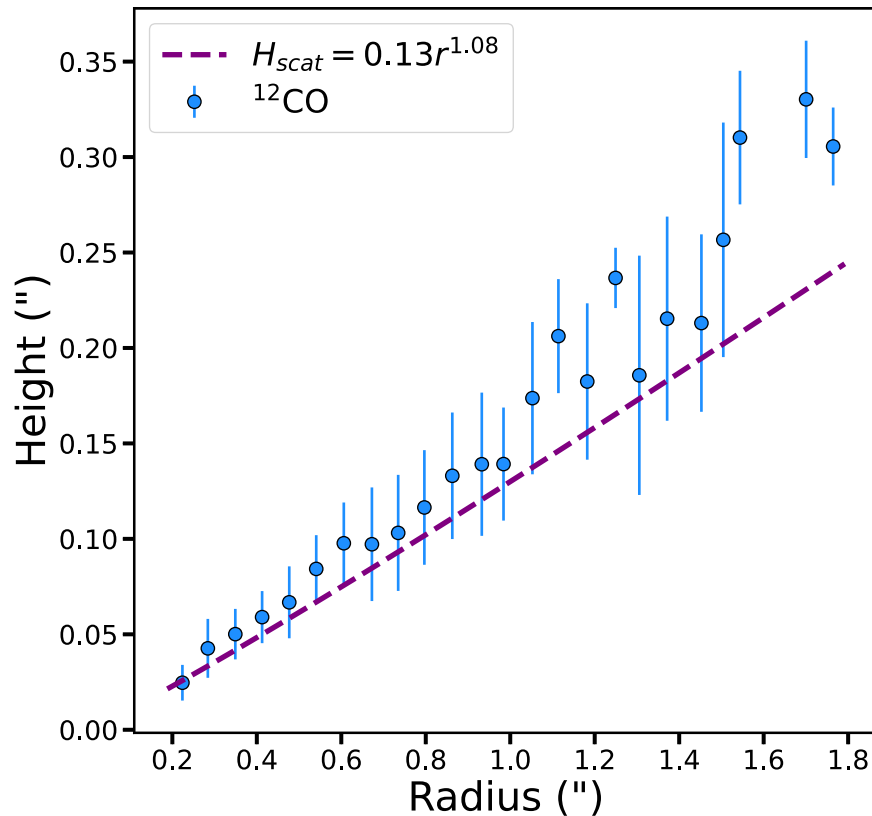


Figure 9. Disk surface height for ^{12}CO , extracted using CO LAYERS (Pinte et al. 2018b), where the uncertainty is taken as the vertical deviation in each bin. The scattered-light emission height is taken to be $H_{\text{scat}} = 0.13 \times r^{1.08}$ from Sissa et al. (2018).

take projection effects into account. We accomplish this by tracing ^{12}CO 's upper emitting layer with the CO LAYERS code presented in Pinte et al. (2018b) and overplotting the scattered-light height prescription from Sissa et al. (2018). In agreement with previous comparisons (Law et al. 2021), Figure 9 shows that ^{12}CO emission and the scattered light arise from a similar height in the disk.

Appendix E An Inner Spiral Seen in SPHERE Observations and Our Fiducial Model

Figure 10 presents a comparison between the SPHERE observations of the inner spiral and synthetic observations produced from our fiducial model. Similar to the observations, our synthetic Q_ϕ r^2 -scaled H -band image shows a large inner

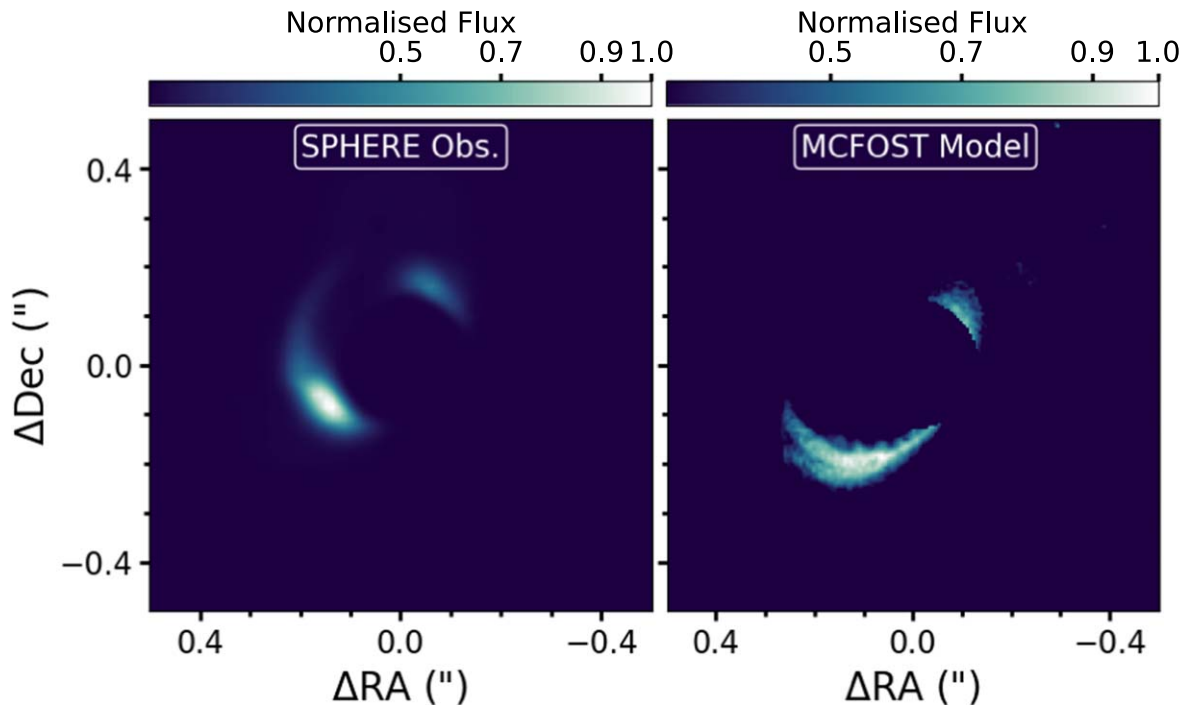






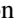
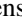
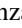





Figure 10. Left: Q_ϕ r^2 -scaled H -band observations. Right: synthetic Q_ϕ r^2 -scaled H -band image produced with MCFOST. For both panels, the flux is normalized to compare the real and synthetic data, and the colorbar is scaled to the power of 4 to solely highlight the bright inner spiral.

spiral arm as well as disk emission on the opposite side of the coronagraph. However, there is an offset in the position angle between the features of the real and synthetic observations.

ORCID iDs

Brodie J. Norfolk  <https://orcid.org/0000-0001-5898-2420>
 Christophe Pinte  <https://orcid.org/0000-0001-5907-5179>
 Josh Calcino  <https://orcid.org/0000-0001-7764-3627>
 Iain Hammond  <https://orcid.org/0000-0003-1502-4315>
 Nienke van der Marel  <https://orcid.org/0000-0003-2458-9756>
 Daniel J. Price  <https://orcid.org/0000-0002-4716-4235>
 Sarah T. Maddison  <https://orcid.org/0000-0001-5827-4088>
 Valentin Christiaens  <https://orcid.org/0000-0002-0101-8814>
 Jean-François Gonzalez  <https://orcid.org/0000-0001-9423-6062>
 Dori Blakely  <https://orcid.org/0000-0001-9582-4261>
 Giovanni Rosotti  <https://orcid.org/0000-0003-4853-5736>
 Christian Ginski  <https://orcid.org/0000-0002-4438-1971>

References

- Artymowicz, P., & Lubow, S. H. 1994, *ApJ*, 421, 651
 Bate, M. R., Bonnell, I. A., & Price, N. M. 1995, *MNRAS*, 277, 362
 Beuzit, J.-L., Feldt, M., Dohlen, K., et al. 2008, *Proc. SPIE*, 7014, 701418
 Booth, A. S., Walsh, C., Kama, M., et al. 2018, *A&A*, 611, A16
 Brittain, S. D., Carr, J. S., Najita, J. R., Quanz, S. P., & Meyer, M. R. 2014, *ApJ*, 791, 136
 Brittain, S. D., Najita, J. R., & Carr, J. S. 2019, *ApJ*, 883, 37
 Bruderer, S., van Dishoeck, E. F., Doty, S. D., & Herczeg, G. J. 2012, *A&A*, 541, A91
 Calcino, J., Hilder, T., Price, D. J., et al. 2022, *ApJL*, 929, L25
 Calcino, J., Price, D. J., Pinte, C., et al. 2019, *MNRAS*, 490, 2579
 Casassus, S., Cárcamo, M., Hales, A., Weber, P., & Dent, B. 2022, *ApJL*, 933, L4
 Casassus, S., & Pérez, S. 2019, *ApJL*, 883, L41
 Cazzoletti, P., van Dishoeck, E. F., Pinilla, P., et al. 2018, *A&A*, 619, A161
 Claudi, R., Maire, A. L., Mesa, D., et al. 2019, *A&A*, 622, A96
 Cornwell, T. J. 2008, *ISTSP*, 2, 793
 de Boer, J., Langlois, M., van Holstein, R. G., et al. 2020, *A&A*, 633, A63
 de Gregorio-Monsalvo, I., Ménard, F., Dent, W., et al. 2013, *A&A*, 557, A133
 Dohlen, K., Langlois, M., Saisse, M., et al. 2008, *Proc. SPIE*, 7014, 70143L
 Dong, R., Liu, S.-y., Eisner, J., et al. 2018, *ApJ*, 860, 124
 Dong, R., Zhu, Z., Rafikov, R. R., & Stone, J. M. 2015, *ApJ*, 809, L5
 Dullemond, C. P., Küffmeier, M., Goicovic, F., et al. 2019, *A&A*, 628, A20
 Fedele, D., Toci, C., Maud, L., & Lodato, G. 2021, *A&A*, 651, A90
 Follette, K. B., Rameau, J., Dong, R., et al. 2017, *AJ*, 153, 264
 Gaia Collaboration, Brown, A. G. A., Vallenari, A., et al. 2021, *A&A*, 649, A1
 Gravity Collaboration, Perraut, K., Labadie, L., et al. 2019, *A&A*, 632, A53
 Garg, H., Pinte, C., Christiaens, V., et al. 2021, *MNRAS*, 504, 782
 Garufi, A., Quanz, S. P., Schmid, H. M., et al. 2016, *A&A*, 588, A8
 Hirsh, K., Price, D. J., Gonzalez, J.-F., Ubeira-Gabellini, M. G., & Ragusa, E. 2020, *MNRAS*, 498, 2936
 Jorsater, S., & van Moorsel, G. A. 1995, *AJ*, 110, 2037
 Kraus, S., Kreplin, A., Fukugawa, M., et al. 2017, *ApJ*, 848, L11
 Law, C. J., Teague, R., Loomis, R. A., et al. 2021, *ApJS*, 257, 4
 McMullin, J. P., Waters, B., Schiebel, D., Young, W., & Golap, K. 2007, in *ASP Conf. Ser. 376, Astronomical Data Analysis Software and Systems XVI*, ed. R. A. Shaw, F. Hill, & D. J. Bell (San Francisco, CA: ASP), 127
 Miley, J. M., Panić, O., Haworth, T. J., et al. 2019, *MNRAS*, 485, 739
 Norfolk, B. J., Maddison, S. T., Pinte, C., et al. 2021, *MNRAS*, 502, 5779
 Paardekooper, S. J., & Mellema, G. 2004, *A&A*, 425, L9
 Pérez, S., Casassus, S., Hales, A., et al. 2020, *ApJL*, 889, L24
 Pinte, C., Harries, T. J., Min, M., et al. 2009, *A&A*, 498, 967
 Pinte, C., Ménard, F., Duchêne, G., et al. 2018b, *A&A*, 609, A47
 Pinte, C., Ménard, F., Duchêne, G., & Bastien, P. 2006, *A&A*, 459, 797
 Pinte, C., Price, D. J., Ménard, F., et al. 2018a, *ApJL*, 860, L13
 Pinte, C., Price, D. J., Ménard, F., et al. 2020, *ApJL*, 890, L9
 Price, D. J., Cuello, N., Pinte, C., et al. 2018b, *MNRAS*, 477, 1270
 Price, D. J., Wurster, J., Tricco, T. S., et al. 2018a, *PASA*, 35, e031
 Ragusa, E., Dipierro, G., Lodato, G., Laibe, G., & Price, D. J. 2017, *MNRAS*, 464, 1449
 Rosotti, G. P., Benisty, M., Juhász, A., et al. 2020, *MNRAS*, 491, 1335
 Shakura, N. I., & Sunyaev, R. A. 1973, *A&A*, 24, 337
 Siess, L., Dufour, E., & Forestini, M. 2000, *A&A*, 358, L24
 Sissa, E., Gratton, R., Garufi, A., et al. 2018, *A&A*, 619, A160
 Stolker, T., Dominik, C., Min, M., et al. 2016, *A&A*, 596, A70
 Teague, R. 2019, *JOSS*, 4, 1220
 Teague, R., Bae, J., Bergin, E. A., Birnstiel, T., & Foreman-Mackey, D. 2018, *ApJL*, 860, L12
 Teague, R., & Foreman-Mackey, D. 2018, bettermoments: A robust method to measure line centroids, v1.0, Zenodo, doi:10.5281/zenodo.1419754
 Toomre, A. 1964, *ApJ*, 139, 1217
 van Holstein, R. G., Girard, J. H., de Boer, J., et al. 2020, IRDAP: SPHERE-IRDIS polarimetric data reduction pipeline, Astrophysics Source Code Library, ascl: 2004.015
 Vioque, M., Oudmaijer, R. D., Baines, D., Mendigutía, I., & Pérez-Martínez, R. 2018, *A&A*, 620, A128
 Walsh, C., Daley, C., Facchini, S., & Juhász, A. 2017, *A&A*, 607, A114
 Weingartner, J. C., & Draine, B. T. 2001, *ApJ*, 548, 296
 Woitke, P., Kamp, I., & Thi, W. F. 2009, *A&A*, 501, 383